Nd isotopic equilibration during channelized melt transport through the lithosphere: a feasibility study using idealized numerical models

Mousumi Roy[1], G. Lang Farmer[2], and Kellen Malone[1]

[1]Department of Physics and Astronomy, University of New Mexico, Albuquerque, NM 87109, USA

[2]Department of Geological Sciences and CIRES, University of Colorado Boulder, Boulder, CO, USA

This is an unpublished manuscript–accepted for publication in G-cubed; Sept 11, 2024

Corresponding author: Mousumi Roy, mroy@unm.edu

Nd isotopic equilibration during channelized melt transport through the lithosphere: a feasibility study using idealized numerical models

Mousumi Roy[1], G. Lang Farmer[2], and Kellen Malone[1]

[1]Department of Physics and Astronomy, University of New Mexico, Albuquerque, NM 87109, USA
[2]Department of Geological Sciences and CIRES, University of Colorado Boulder, Boulder, CO, USA

Key Points:

- Trace elements in primitive basalts from southwest North America suggest both asthenosphere- and lithosphere-related signatures
- Open system interactions between ascending channelized melts and wallrock may affect the trace element composition of erupted basalts
- 1D transport models quantify the role of diffusion and wallrock assimilation to produce significant Nd isotopic shifts over 10 km of transport

Corresponding author: Mousumi Roy, mroy@unm.edu

Abstract

This study is motivated by the observed variability in trace element isotopic and chemical compositions of primitive (SiO_2 <52 wt %) basalts in southwest North America (SWNA) during the Cenozoic transition from subduction to extension. Specifically, we focus on processes that may explain the enigmatic observation that in some localities, basalts with low Ta/Th, consistent with parental melts in a subduction setting, have ε_{Nd} signatures consistent with continental lithospheric mantle (CLM). In locations with the oldest CLM (Proterozoic and Archaean), Cenozoic basalts with low Ta/Th have ε_{Nd} well below zero. We model channelized magma transport through the CLM using simple 1D transport models to explore the extent to which diffusive and reactive mass exchange can modify Nd isotopic compositions via open system melt-wallrock interactions. For geologically reasonable channel spacings and volume fractions, we quantify the reactive assimilation rates required for incoming melt with a different ε_{Nd} than the wall-rock to undergo a substantial isotopic shift during ≈10 km channelized melt transport. In the presence of grain boundaries, enhanced diffusion between melt-rich channels and melt-poor surrounding rock contributes to isotopic equilibration, however this effect is not enough to our models suggest that requires a significant contribution from reactive assimilation of wall-rock. Additionally our models support the idea that the observed covariability in Ta/Th and ε_{Nd} in Cenozoic basalts cannot be attributed to transport alone and must reflect the transition from subduction-related to extension-related parental melts in SWNA.

Plain Language Summary

Over the past half century, the abundances and isotopic ratios of trace elements such as Nd in basalts have been widely used to infer aspects of the source region where mantle melting occurs. This assumes that when the mantle melts, trace element characteristics of source rocks are inherited by the generated melts and these are not further modified as melts ascend through the tectonic plate (lithosphere) to be erupted as basalt. We reassess this assumption inspired by enigmatic observations from southwest North America, where basalts that have undergone minimal processing (primitive basalts), show trace element characteristics of both the mantle lithosphere and of the asthenosphere. We use 1D transport models to show that melts moving in channels through the lithosphere may undergo significant trace element changes by interacting with the walls as they ascend, thereby explaining the observations with geologically-reasonable scenarios.

1 Introduction

Over the past half century, the chemical and isotopic compositions of continental basalts have been widely used to infer aspects of the physical and chemical evolution of the continental lithospheric mantle (CLM) and underlying asthenosphere. An implicit assumption in this approach is that, after correction for crustal contamination, primitive basaltic rocks have incompatible trace element ratios and radiogenic isotopic compositions inherited from their mantle source rocks, the latter defined here as the portion of the upper mantle in which melting initiated. However, incompatible element and isotopic ratios of continental basalts need not reflect those values inherited from a single mantle source region. For example, mantle derived melts that ascend to the surface are likely aggregates of multiple parental melts that might themselves have different sources (e.g., Stracke, 2021). Even basaltic melts derived from a single source may be compositionally modified by open system interactions with their surroundings during extraction, migration and ascent through the mantle (Navon & Stolper, 1987; Stracke & Bourdon, 2009; Liu & Liang, 2017).

In this paper we are concerned with the latter possibility. A need to reevaluate the role of mantle wall rock interaction in influencing basalt trace element and isotopic compositions has arisen from a recent reassessment of the extensive chemical and isotopic data available from Cretaceous and younger basaltic rocks in southwestern North America (SWNA). It has long been recognized in SWNA that many basalts are characterized by relatively non-radiogenic initial $^{143}Nd/^{144}Nd$ ratios, and $\varepsilon_{Nd}(T) < 0$, interpreted as evidence that their parental melts were sourced in low $\varepsilon_{Nd}(T)$ Precambrian CLM (Fig 1a; Menzies et al., 1983; Fitton et al., 1988). (In the following, we only refer to time-corrected $\varepsilon_{Nd}(T)$ values, and will drop the (T) for simplicity.) But based on the entire compositional data set now available, it is now apparent that negative ε_{Nd} basaltic rocks can be subdivided into two distinct groups based on incompatible high field strength element ratios, specifically Ta/Th. One Ta/Th group corresponds to low ε_{Nd} basalts with Ta/Th < 0.2, and with strongly correlated Ta and Th abundances ("low" Ta/Th group) that occur throughout SWNA (Farmer et al., 2020). Low Ta/Th values with strongly correlated Ta and Th abundances are characteristic of mafic to intermediate composition volcanic rocks in oceanic and continental arcs worldwide, and are generally interpreted as values inherited from melting of asthenospheric mantle wedge fluxed by volatiles derived from underlying oceanic lithosphere during active subduction (Fig 1b). The sec-

ond low ε_{Nd} group has intermediate Ta/Th values, typically from 0.2 to 0.6, with decoupled Ta and Th abundances ("intermediate" Ta/Th group). Volcanic rocks with intermediate Ta/Th values are rare in oceanic settings, but common in SWNA where they typically occur after low Ta/Th group volcanism, although the absolute timing of the end of low Ta/Th and the onset of intermediate Ta/Th volcanism varies with geographic position. Intermediate Ta/Th volcanism in SWNA has been attributed to in situ melting of CLM metasomatized by fluids derived from oceanic lithosphere during low angle subduction that affected SWNA in the Late Cretaceous and Early Cenozoic (Fig 1b; Farmer, 2022; Farmer et al., 2020). The conundrum is that while low Ta/Th basaltic rocks are attributed to melting in high ε_{Nd} ($\varepsilon_{Nd} > 0$) asthenosphere and intermediate Ta/Th rocks represent in situ melting of low ε_{Nd} CLM, both sets of volcanic rocks have low ε_{Nd} values (Fig 1a). While a low ε_{Nd} value may arise from time-integrated effects of subduction-related modification of the asthenosphere (McCulloch & Gamble, 1991; Peate et al., 1997; Chauvel et al., 2008), Late Cretaceous basaltic rocks (with both low and intermediate Ta/Th values) in SWNA have ε_{Nd} values that correlate with the age of underlying Precambrian continental lithosphere: those underlain by Archean lithosphere have consistently lower ε_{Nd} than those underlain by lithosphere of Paleoproterozoic age (Fig 1a). This observation is still best explained by the derivation of Nd in these rocks from ancient CLM. One way to generate basalts that reflect both sub-lithospheric low Ta/Th magmas and a CLM-like Nd isotopic signature may be through interaction and partial-equilibration of high ε_{Nd} parental magmas during transport through thick, low ε_{Nd} CLM. Assessing this scenario is the goal of the current work. Motivated by the observations above, we test the possibility that lithospheric or sub-lithospheric parental melts may experience variable equilibration with thick, ancient CLM during transport (Fig. 1b).

The effects of chemical and isotopic disequilibrium during melt generation and segregation in the mantle have been explored in numerical models for mid-ocean ridge and ocean island settings (e.g., Iwamori, 1993; Hauri, 1997; Kenyon, 1993). More recently, numerical models of disequilibrium reactive transport in porous flow highlight a richness of behavior that arises from diffusive exchange, particularly when it comes to interpreting trace element compositions (e.g., Oliveira et al., 2020, and refs within). This work builds upon these previous studies, particularly the approach of Hauri (1997), with the specific goal of considering the effects of chemical and isotopic disequilibrium during channelized transport of melts through the CLM. It is clear from detailed geochemical and

petrologic characterization of exhumed CLM (e.g., in the Lherz and Ronda massifs) that isotopic, chemical, and thermal disequilibrium may exist across contacts between channelized melts and their surroundings (LeRoux et al., 2007, 2008; Soustelle et al., 2009). Here we use the term "channel" to denote a spatially-limited melt-rich zone with a higher-than-ambient melt volume fraction (porosity), surrounded by material that is melt-poor (wall rock). Magma transport through the CLM is likely channelized at the macroscopic (10^{-1} to 10^{1} m scale) (e.g., Katz et al., 2022, and refs within), probably in systems of ephemeral channels, and we consider the field relations in exhumed peridotite massifs to represent a primary mode of melt transport in the lower CLM (e.g., LeRoux et al., 2007, 2008; Soustelle et al., 2009). The models presented here are highly idealized in that they do not address the origin of channelization and parameterize averaged channel geometries and average motion of melt through the lower CLM. Our models also ignore thermochemical disequilibrium in major element compositions between the wallrock and melt-rich channels. Instead, the mass exchange in our models places limits on one process in particular, namely, trace element exchange by self-diffusion. They are, therefore, far from a complete representation of disequilibrium in channelized transport. Our purpose therefore is to use these calculations as a feasibility study to show that partial equilibration across channel walls may explain the conundrum in SWNA basalt trace element and Nd isotopic compositions described above. The open-system interactions we model concern Nd isotopic equilibration during transport and speculate on ways in which a CLM-like Nd isotopic signature may be imparted to melt within channels, while simultaneously preserving sublithospheric Ta/Th ratios.

We focus on diffusion and reaction (assimilation/precipitation) as two primary mass transfer mechanisms between channels and their surroundings, and explore the role of each. To investigate diffusive exchange between wall rock and channels, we consider a scenario where diffusion is strongly controlled by the configurational anisotropy that arises from the presence of grain boundaries in the wall material. Grain boundaries within the wallrock should be associated with both segregation of incompatible elements (Hiraga et al., 2004; Alard et al., 2022; Demouchy & Alard, 2021) and enhanced diffusive transport (Hiraga et al., 2007a,b; Dohmen & Milke, 2010). We show that this leads to enhanced effective diffusivity, allowing diffusive exchange to reach further into wall rock (e.g., Jaseliūnaitė et al., 2022). Diffusive equilibration between an ascending, sublithosphere derived melt and surrounding CLM (when the two have a large initial isotopic contrast), however, can-

not account for the Nd isotopic composition of basalts in SWNA. Instead, the observations require a role for mass transfer (via dissolution/precipitation) between wall rock and melt. Our simplified models ignore major-element chemical compositional variability within and between melt-rich and melt-poor parts of the system, building on Hauri (1997) (as described below). Our goal is to explore the regimes of behavior within a geologically-relevant parameter space of channel spacing, volume fraction, fluid velocity, and likely Nd chemical and isotopic contrast across channel walls. Recognizing the limitations of an idealized model, we focus here on the degree of equilibration that may be established in 10 km of transport, a fraction of the CLM thickness. Our work establishes limits on the role of channel-wall diffusive exchange and reactive exchange, allowing us to assess the potential importance of isotopic shifts by mechanisms not included here, such as in-situ CLM melting, in generating low-silica basalts with CLM-like negative ε_{Nd}.

2 Idealized transport model

We construct an idealized 1D schematic model where open system interactions in a real-world complex channel network (Fig. 2a) are abstracted into a 1D domain containing melt-rich channels with moving material (here denoted as "fluid"; subscript f) and melt-poor stationary wall rock ("solid"; subscript s); Fig. 2b. Our model is based on similar 1D approaches(Hauri, 1997; Roy, 2022, and references therein), however our work includes mass transfer (diffusive and reactive exchange) perpendicular to channel walls and diffusion along the transport direction within each of the fluid and solid domains. We use a set of modified advection-diffusion equations:

$$\frac{\partial C_f(x,t)}{\partial t} + v\frac{\partial C_f(x,t)}{\partial x} = -\frac{(1-\phi)\rho_s}{\phi\rho_f}\frac{1}{\tau_{ex}}(KC_f(x,t) - C_s(x,t)) + D_f\frac{\partial^2 C_f(x,t)}{\partial x^2} \quad (1)$$

$$\frac{\partial C_s(x,t)}{\partial t} = \frac{1}{\tau_{ex}}(KC_f(x,t) - C_s(x,t)) + D_s\frac{\partial^2 C_s(x,t)}{\partial x^2} \quad (2)$$

Here transport is assumed to be dominantly 1D (along $+\hat{x}$) with average relative velocity, v, between the material within the channels and outside (in a reference frame stationary with respect to the channel walls; Fig. 2b). $C_f(x,t)$ and $C_s(x,t)$ represent the total concentration (mol/m^3) of the relevant isotopes of a trace element, in this case Nd, within and outside channels. The terms on the right hand sides of Eqns (1) and (2) rep-

resent: (i) material exchange across channel walls and (ii) diffusion within either the channel or the solid walls along the transport direction. The exchange term assumes that interaction across channel walls depends linearly on the degree of thermodynamic disequilibrium ($KC_f(x,t) - C_s(x,t)$), where K is the mineral-melt partition coefficient, following Hauri (1997) and Kenyon (1993) (see also Roy, 2022, for a similar treatment of thermal disequilibrium). The rate of mass exchange across channel walls depends on an exchange timescale, τ_{ex}, which depends upon the exchange mechanism (to be defined below). Other parameters include: the average channel spacing, d, and the average volume fraction of channels, ϕ, fluid and solid densities, ρ_f and ρ_s, and spatially uniform diffusion constants, D_f and D_s. Parameters and their values used here and elsewhere are listed in Table 1. We emphasize here that ϕ is the channel volume fraction, and not the fraction of melt in porous flow within the melt-poor channel walls. The range of values of ϕ considered, 5-20%, are not well constrained but are comparable to those in exposed peridotite massifs (e.g., Soustelle et al., 2009; LeRoux et al., 2007). We assume that the effective diffusion coefficients (D_f, D_s) and bulk mineral-melt partition coefficient K are nearly indistinguishable for isotopes with high atomic number (Watkins et al., 2011, 2014, 2017), so these coefficients are assumed to be equal for all Nd isotopes. The bulk mineral-melt partition coefficient K used in this work is calculated from the partition coefficients for Nd in Salters & Longhi (1999) applied to the peridotite composition listed in Farmer et al. (2020).

To treat isotopic equilibration, we define $C(x,t) = C^{144}(x,t) + C^{143}(x,t)$, and the relative mol fraction of ^{144}Nd as $f \equiv C^{144}(x,t)/C(x,t)$. Substituting these into Eqns (1) and (2) leads to the following expressions for the evolution of f in the fluid and solid, which are similar in form to (Johnson & DePaolo, 1994) (derivation of Eqns (3) and (4) in Supp. S1):

$$\frac{\partial f_f}{\partial t} + v\frac{\partial f_f}{\partial x} = \frac{1}{C_f}\left(-\frac{(1-\phi)\rho_s}{\phi\rho_f}\frac{1}{\tau_{ex}}C_s(f_f - f_s) + 2D_f\frac{\partial f_f}{\partial x}\frac{\partial C_f}{\partial x} + D_f\frac{\partial^2 f_f}{\partial x^2}C_f\right) \quad (3)$$

$$\frac{\partial f_s}{\partial t} = \frac{1}{C_s}\left(\frac{1}{\tau_{ex}}KC_f(f_f - f_s) + 2D_s\frac{\partial f_s}{\partial x}\frac{\partial C_s}{\partial x} + D_s\frac{\partial^2 f_s}{\partial x^2}C_s\right) \quad (4)$$

This system of Eqns. (1-4) is applied to Nd in this study, but may be generally relevant to trace element exchange, where the concentration of the element is small. Here, we assume that any gradients in major element compositions and chemical activities will

not affect diffusion of isotopes of Nd, a simplification further discussed below (but see Watkins et al., 2014). Additionally, by constraining our attention to ^{144}Nd and ^{143}Nd, we are assuming that gradients in the concentration of the other isotopes of Nd may be neglected assuming they will equally affect both isotopes in consideration (e.g., Du et al., 2022).

2.1 Effective diffusivity in channel walls

The diffusivities employed here (Table 1) are based on the self-diffusivity of Nd (Lesher, 2010; Zhang, 2010), assuming that isotopic fractionation between ^{144}Nd and ^{143}Nd due to mass-dependent diffusivity is negligible (a power-law dependence on the mass ratio, e.g., Watkins et al., 2014). Although lattice (grain) diffusivity, D_x, for Nd is generally very low ($D_x = 10^{-19}$ to 10^{-17} m^2/s; VanOrman et al. (2002); Ganguly et al. (1998)), it has long been recognized that the effective diffusivity, D_s, for peridotite (assumed channel wall rock) as a polycrystalline aggregate may be significantly larger. There are likely two mechanisms for this enhanced diffusion which governs exchange between channels and their surrounding walls: high diffusivity within grain boundaries and segregation of incompatible elements into inter-granular regions. In polycrystalline aggregates, the presence of grain boundaries may increase the effective diffusivity of Nd by 10^3-10^6 above the lattice value (Hiraga et al., 2007a,b), possibly up to a factor of 10^8 (Shewmon, 1989, although this is not well-constrained for mantle minerals; J. van Orman, pers. comm.). Additionally, segregation of incompatible elements into high-diffusivity grain boundaries can also play an important role in enhancing their mobility (Reddy et al., 2020; Demouchy & Alard, 2021).

We suggest that an additional (geometry-dependent) effect arises from the configurational anisotropy due to enhanced diffusion within grain boundaries. We demonstrate this in a 2D mesoscopic model, following Jaseliūnaitė et al. (2022), to illustrate the first-order effect of the presence of grain boundaries in an idealized model aggregate based on an actual peridotite thin-section (Fig 3). Hiraga et al. (2007b) suggests that the effective (bulk) diffusivity of the aggregate should be $D_s \approx D_x + s(3w/\delta)D_{GB}$, where D_x is the lattice (grain) diffusivity, D_{GB} is the diffusivity of the inter-grain regions, s is a segregation factor associated with enhanced storage of incompatible elements at grain boundaries, w is the grain boundary width, and δ is the average grain size. We assume that diffusivity in grain boundaries is enhanced by a factor $E = D_{GB}/D_x$ over the lat-

tice value. If $E = 10^4$ (within the expected range $10^3 - 10^6$), then for aggregates with grain boundary width w on the order of 10^{-9} m and grain size d around 1 mm, Hiraga et al. (2007b) suggests that $s(3w/d) \approx 10^{-2}$ so that the effective diffusivity D_s should be a factor 10^2 larger than D_x. Using $E = 10^4$ for the model aggregate in Fig 3a, we find that the actual effective diffusivity D_s is around $\approx 5{\times}10^2$ larger than D_x, driven mainly by the effect of anisotropic diffusion in the presence of grain boundaries. The configurational anisotropy of high-diffusivity grain boundaries increases the wall-rock volume sampled by diffusive exchange (Fig 3c). A grain boundary enhancement of $E = 5{\times}10^4$ leads to an effective diffusivity of $D_s \approx 10^3 D_x$. In the following transport model, therefore, we take a conservative approach and consider a maximum value for the effective diffusivity in the channel walls of $D_s = 2 \times 10^{-17}$ m^2/s, about 200 times larger than the lattice diffusivity (VanOrman et al., 2002; Ganguly et al., 1998), but suggest that further work is needed to assess anisotropy-enhanced effective diffusivity.

2.2 Exchange time scale τ_{ex} and Dahmköhler number

To solve the system of Eqns (1-4), we non-dimensionalize and use a finite-difference approach (Supplementary Text S3), parameterizing the model with a Damköhler number,

$$Da = \frac{(1-\phi)\rho_s}{\phi\rho_f}\frac{\tau_{ad}}{\tau_{ex}} \tag{5}$$

a dimensionless ratio of the time scale of melt advection $\tau_{ad} = L/v$ (L is the domain length) to the time scale of exchange between the fluid and solid τ_{ex}. The latter time scale depends upon the mechanism of mass transfer between material in the channels and the surrounding wall rock. For diffusion the relevant timescale is $\tau_d = d^2/(\alpha D_s)$ (Hauri, 1997), where α is a flow coefficient (=10 for channelized flow; e.g., Bodinier et al., 1990; Hauri, 1997). For reactive exchange, the timescale is instead $\tau_r = d/2R$, where R is a linear dissolution/precipitation rate (Hauri, 1997).

When both mechanisms are present, they each contribute an independent term proportional to the degree of disequilibrium on the right hand side of Eqns (1 to 4), so that the Dahmköhler number Da depends on an effective exchange timescale, τ_{ex}, where $1/\tau_{ex} = 1/\tau_r + 1/\tau_d$, the harmonic mean of the timescale of both processes. The harmonic mean is appropriate when the processes are independent and the equilibration is simultaneously due to the lower-rate process (diffusion) and the higher-rate process (reaction): in

effect, the two mechanisms are like resistors "in-parallel", so the effective timescale is not an arithmetic mean but rather a harmonic one. Through the timescale for diffusive exchange, τ_d, Da depends on the effective diffusivity in the wallrock, D_s, discussed above. Strictly, this depends on the diffusing species, and in this work we confine our attention to trace elements such as Nd. Da is a measure of the intensity of the fluid-solid mass exchange across channel walls within the domain relative to advection within the channels. For example, for a fixed volume fraction of channelized melt, ϕ, if the channel spacing, d, is decreased then the interphase contact area per unit volume increases (Fig. 2b), decreasing τ_{ex} and increasing Da, leading to more vigorous exchange across channel walls (see also Supplementary Fig. S1).

2.3 Initial and boundary conditions

We study the transport Eqns (1-4) subject to initial and boundary conditions as follows: initially the moving material in the channels is in equilibrium with the walls ($KC_{f0} = C_{s0}$), with no time variations (steady state). Then (at $t = 0$), the channelized material entering the domain at the inlet ($x = 0$) is subject to an imposed smoothed step-perturbation in chemical and isotopic composition (Fig. 2c). The perturbation in isotopic and chemical composition of the fluid at the inlet ($x = 0$) begins at time $t = 0$, but is associated with a rise time w_0, the perturbation time scale. Therefore, for a given w_0, model behavior will be a strong function of the dimensionless time $\tau' = w_0/\tau_{ex}$. Following a transient response governed by two dimensionless numbers Da and τ', therefore, the system eventually returns to steady-state (no time-variations).

Characteristic values for initial and perturbed Nd chemical compositions are based on observations of mantle xenoliths and from Cenozoic basalt samples from SWNA (Supp. S2; Fig. S3). Initially, $KC_f(x,0) = C_s(x,0)$ and $f_f(x,0) = f_s(x,0)$, where we assume $C_s(x,0) = C_{s0} = 1$ ppm and initial $\varepsilon_{Nd,f}(x,0) = \varepsilon_{Nd,s}(x,0) = -2$ (Table 1). We solve for the response of the system to a smoothed step-change imposed in both $C_f(0,t)$ and $\varepsilon_{Nd,f}(0,t)$ at the inlet ($x = 0$) at $t = 0$ (see Supp. S3 for functional form). The perturbation in $\varepsilon_{Nd,f}(0, t > 0)$ changes the fluid value from -2 to +8 and the perturbation in $C_f(0, t > 0)$ changes from $1/K$ ppm to 30 ppm (Table 1; Supp. S2).

3 Results

To highlight the role of channel-wall mass exchange in determining the evolution of fluid composition, we present our results tracking the chemical and isotopic evolution of specific parcels of fluid, in a (Lagrangian) reference frame fixed to each parcel (cf. Farmer & DePaolo, 1997). (The subscript l indicates quantities in a given fluid parcel, e.g., C_{fl}, while quantities without l are in an Eulerian frame, e.g, C_f. See also Supplementary Fig S3 for Eulerian profiles.) Following the step-perturbation, we track 3 parcels of fluid, $fluid_1$, $fluid_2$, and $fluid_3$, entering the domain at various times t_1, t_2, and t_3 (Fig. 2c). To quantify the degree of isotopic equilibration a parcel may undergo after, say, 10 km of transport, we define Δ_{10},

$$\Delta_{10} = 1 - \frac{(\varepsilon_{Nd,lf} - \varepsilon_{Nd,ls})_{x=10\ km}}{(\varepsilon_{Nd,lf} - \varepsilon_{Nd,ls})_{x=0\ km}} \tag{6}$$

where $(\varepsilon_{Nd,lf} - \varepsilon_{Nd,ls})$ is the (local) contrast between a fluid parcel and the solid wall adjacent to it. (In Figs 4 and 5a, the reported Δ_{10} values are for the $fluid_1$ parcel in Fig. 2c.)

Three regimes of behavior are evident, governed by the dimensionless Da and τ' numbers, as follows (Fig. 4): (I) small Da and τ', with minimal to no equilibration and exchange where chemical and isotopic contrasts between the fluid parcel and its surroundings are maintained over large transport distances, (II) intermediate Da and τ', with substantial exchange and partial equilibration over the model domain; and (III) large Da and τ', characterized by strong transverse mass exchange leading to (spatially-varying) local equilibrium across channel walls.

In regime I, $\varepsilon_{Nd,l}$ values in both the fluid and the solid are barely modified after 10 km of transport, $\Delta_{10} \approx 0$ (no equilibration; Fig. 4a) and the imposed disequilibrium between the fluid and the solid is preserved. By contrast in regime III, the exchange time scale is much smaller than the advection time scale so that the fluid and the solid are in nearly instantaneous local equilibrium: the solid composition (unphysically) tracks the perturbed fluid compositions as the parcel interacts with and passes the solid ($\Delta_{10} < 0$; Fig. 4d). After $fluid_1$ has modified the solid domain, $fluid_2$ enters 5 Kyrs later and (unlike $fluid_1$) does not interact with unmodified solid upon entering the domain, but has to traverse several km before reaching the unmodified solid portion of the domain (e.g., Fig. 4d). The same process happens for $fluid_3$, which enters 5 Kyrs after $fluid_2$, further increasing the distance needed to reach unmodified solid. Subsequent fluid parcels

would continue needing more and more travel time to reach unmodified solid until the whole domain has been modified to the perturbation composition and any new fluid parcels entering the domain will have the same composition at the end of the domain as that at the inlet. The instantaneous equilibration in regime III (for high Da and τ' in Fig. 4d) is likely to be unphysical for application to the real world. In this regime (particularly for large τ' where the perturbation timescale is long compared to exchange), the 1D models would allow infinite exchange, whereas in the real (3D) world equilibration fronts moving perpendicular to channel walls may meet and exhaust unmodified wall-rock, limiting the amount of possible equilibration. Both regime I and regime III in the long-time limit are associated with fluid compositions that remain unchanged through the domain.

Regime II on the other hand is associated with partial equilibration during transport: the imposed disequilibrium between incoming fluid parcels and the surrounding solid persists, but the degree of disequilibrium decreases with transport ($0 < \Delta_{10} \leq 1$; Fig. 4b-c). Like regime III, the solid is modified by each passing fluid parcel, so subsequent fluid entering the domain will not exit the domain with the same composition as fluid entering prior or after it. These regimes are summarized in a "phase diagram" of model behavior in the Da and τ' space (Fig 5a; for simplicity, we report Δ_{10} for $fluid_1$ in Fig. 2c, which enters the inlet with $\varepsilon_{Nd,fl} = +8$). Generally, for partial Nd isotopic equilibration (regime II) between basaltic melts ($\varepsilon_{Nd} = +8$, ≈ 30 ppm Nd) and CLM (here $\varepsilon_{Nd} = -2$, 1 ppm Nd), we require $Da > 10$ (Fig 5a). As demonstrated in Fig 5b, if we use $D_s = 10^{-17}$ m^2/s as a reasonable solid diffusivity, $Da \geq 10$ may be achieved for a wide range of geologically-reasonable parameters: e.g., $Da = 10$ for $v = 1$ m/yr, $d = 1$ m, and a reaction rate of $R \approx 1.5 \times 10^{-13}$ m/s).

4 Discussion

The results above suggest that Nd isotopic equilibration during channelized transport maybe be categorized into three regimes of behavior as a function of the dimensionless Dahmköhler number Da and perturbation timescale τ' (Fig. 5). This categorization also appears in other 1D melt transport models (Hauri, 1997; Kenyon, 1993) and in isotopic advection-reaction models for hydrothermal fluids moving through rock (Farmer & DePaolo, 1997), suggesting they are a generic feature of 1D fluid-solid advection-diffusion/reaction transport models. The applicability of these 1D results, and previous 1D approaches (Hauri,

1997; Kenyon, 1993), to magma transport within the CLM is limited as the approach is confined to a single transport direction with constant relative velocity v and constant geometry and material properties within the domain. The 3D effects of channel geometry (sinuosity, orientation, etc.) are combined into two scalars, d and ϕ, the channel spacing and volume fraction (cf. Roy, 2022). We mitigate this to some extent in this study, however, by confining our attention to short transport distances (≈ 10 km) and channel spacings $d \geq 1$ m, even though geologic observations support the idea of channelized flow at the sub-meter scale (e.g., Braun & Kelemen, 2002; Liang et al., 2010; LeRoux et al., 2008). We recognize that over ≈10 km of transport the ambient temperature in the CLM may vary by several tens of degrees (e.g., equilibrium thermal gradient of 5^oC/km) and one might expect thermally-driven variations of material parameters (D_s, D_f, K; e.g., Van Orman et al. (1998)). On the other hand, transient heating due to melt transport (e.g., Roy, 2022) may mitigate this effect. The lack of combined heat and mass-transfer across channel walls is a limitation of these 1D models, and beyond the scope of this study. Therefore, the models above are best regarded as representing the time-averaged effects of a stochastic transport process (e.g., an ensemble of ephemeral dikes or channels) within the CLM, when transport in a particular direction dominates over others. By considering $d \geq 1$ m, we adopt a conservative approach: our estimates of the degree of isotopic equilibration is likely a lower bound, as sub-meter spacings would likely lead to higher interphase contact area per unit volume and therefore more exchange across channel walls. Unlike melt distributed at the grain-scale (Hirth & Kohlstedt, 2003), the effect of the melt-rich channels on the overall rheology of the CLM is not well-understood, so it is difficult to quantify how the range of channel volume fraction ϕ here would affect the overall deformation of the lowermost CLM. Furthermore, processes such as reactive exchange via dissolution/precipitation may alter the channel geometry parameters (d and ϕ, assumed constant here). In this model, we ignore such feedbacks. With these caveats in mind, three robust results emerge for models with geologically reasonable channel spacings $d = 1$ to 100 m, channel volume fractions $\phi = 0.05$ to 0.2, and a conservative estimate for the effective Nd diffusivity in the channel walls $D_s = 10^{-17}$ m^2/s, as follows.

First, partial Nd isotopic equilibration during channelized transport within the CLM is achievable for $Da \geq 10$ for a broad range of perturbation timescales (regime II in Figs 4b and 5a). This situation is likely if the dimensionless linear reaction (assimilation) rate

R/v is higher than 2×10^{-6} to 10^{-5}, which for a channel flow rate of v =1 m/yr leads to $R = 1.5 \times 10^{-13}$ m/s (Fig. 5b). This conclusion is unchanged even if $D_s = D_x = 10^{-19}$ m^2/s is assumed, as the diffusive timescale is much longer than that for reaction so the exchange timescale, and therefore Da, is more strongly controlled by τ_r than τ_d. While the simulations above assume an in-channel advective velocity $v = 1$ m/yr, we do not specify the physical orientation of the transport direction ($+\hat{x}$). The results are therefore a first-order estimate to the degree of isotopic equilibration expected across channels of any orientation. Vertical melt ascent rates may however be up to 10^1 m/yr (e.g., Katz et al., 2022) and if transport direction is dominantly vertical with $v = 10$ m/yr instead of 1 m/yr, (for $d = 1$ m, $\phi = 0.1$, $R = 1.5 \times 10^{-13}$ m/s) Da would be reduced from 10 to 1. In this case, reaching regime II would require a larger reaction rate, $R = 10^{-12}$ m/s. To put these reaction rates in context, the kinetics of transient crystal dissolution and precipitation driven by chemical disequilibrium in a binary or ternary melt system (Liang, 2003) predict $R \approx 2 \times 10^{-11}$ m/s (for diffusion-in-solid limited dissolution) up to $R \approx 2 \times 10^{-8}$ m/s (for diffusion-in-melt limited dissolution). Linear reaction rates $R = 10^{-12}$ to 10^{-13} m/s needed to achieve Da=10 for melt ascent rates v=1 to 10 m/yr (e.g., for d=1 m, and ϕ=0.1; Fig 5b), fall well below kinetically-constrained dissolution/precipitation rates. Therefore, partial Nd equilibration in the presence of chemical and isotopic disequilibrium between infiltrating melts and their surrounding wallrock, a hallmark of regime II behavior in our models (Figs 4 & 5), is geologically feasible.

Second, if $Da \geq 10^2$, partial equilibration by open-system interactions over 10 km of transport is sufficient to achieve $\Delta_{10} \geq 0.5$ (Fig 5a). For a fluid parcel that enters the CLM with a maximum initial isotopic contrast of +10 epsilon units (e.g., for $fluid_1$ in our models $\varepsilon_{Nd,f0} = +8$ and $\varepsilon_{Nd,s0} = -2$), this is equivalent to an isotopic shift of 5 epsilon units. The transport distance needed to change the fluid $\varepsilon_{Nd,f}$ by a similar amount in subsequent fluid parcels, however, would be larger as the surrounding solid equilibrates towards the perturbed fluid value from earlier fluid parcels, thus decreasing the degree of disequilibrium between later-entering fluid parcels and the wallrock.

Third, returning to the observations of Cenozoic basalts in SWNA, this process would predict a temporal shift in ε_{Nd} in primitive basalts through time from low to high values, as corroborated by observations in specific localities such as the southern Rio Grande Rift (e.g., Fig. 17 in Farmer et al., 2020). Additionally, the CLM in SWNA has under-

gone significant thinning in Cenozoic time, which also drives the temporal shift in ε_{Nd}. For primitive basalts with subduction-related low Ta/Th but CLM-like negative ε_{Nd} (Fig 1a), our models suggest that one explanation may be a much lower Da for Ta and/or Th exchange (e.g., regime I, no equilibration) than for Nd (regime II, partial equilibration) during transport of these rocks. However, it is difficult to envision a scenario where trace element exchange is significantly slower for Ta and/or Th vs for Nd in the presence of a given channel network geometry, with wallrock-channel mass transfer via reactive assimilation and diffusive processes. An alternate explanation is that the infiltrating asthenospheric melts and lowermost CLM had similar, low Ta/Th values (< 0.2) but the former had higher ε_{Nd} at the outset. Typical upper mantle has a Ta/Th ~ 1 (Farmer et al., 2020) but there is evidence that subarc asthenosphere, even if initially involved in flux melting during active subduction, can be subsequently refertilized through interaction with low Ta/Th magmas as active subduction proceeds (Chin et al., 2014). This process imparts LREE enrichments and low Ta/Th values to the mantle. After cessation of subduction, and stabilization in continental lithosphere, this mantle develops increasingly negative ε_{Nd} values and isotopic disequilibrium with underlying convecting upper mantle, while retaining low Ta/Th values. If at least the base of the Precambrian mantle lithosphere in SWNA evolved In this fashion, then low Ta/Th asthenosphere-derived melts infiltrating the low Ta/Th base of the CLM during the Late Cretaceous and Cenozoic would have Nd isotopic compositions in disequilibrium across channel walls and therefore partially equilibrate, without substantially modifying the melt Ta/Th values.

The idea that channelized melt and wallrock experience different degrees of disequilibrium in the Nd isotopic and Ta/Th systems is supported by the observation that, in some parts of SWNA, the transition from low to high ε_{Nd} (and the correlated transition from low to high Ta/Th) occur progressively in time (Farmer et al., 2020; Farmer, 2022). In a subduction setting, where the upper plate CLM is infiltrated by high ε_{Nd} and low Ta/Th melts produced in the mantle wedge, our models would predict that regime III behavior is required for a progressive modification of the wallrock leading to a temporal transition from low to high ε_{Nd}. However, the end product of such progressive modification of wallrock would generate basalts with high ε_{Nd} and low Ta/Th, in contradiction with the observations (Fig 1a). This effectively rules out regime III behavior as an explanation for the correlated transition in Nd isotopes and in Ta/Th (Fig 1a). While

the simultaneously low ε_{Nd} and low Ta/Th may be explained by partial Nd isotopic equilibration between a low Ta/Th (metasomatized) ancient CLM high Ta/Th (regime II behavior, as we have argued above), our models imply that protracted transport of melts derived from the mantle wedge through the CLM cannot explain the correlated increase in both ε_{Nd} and Ta/Th in SWNA alkali basalts. Instead, a different process must be invoked, namely, that the Ta/Th composition of infiltrating melts changes through time, from low to high values. A geologically-reasonable scenario would be that, as SWNA underwent a transition from subduction to Neogene CLM thinning and extension, processes generating parental melts changed from flux-melting (low Ta/Th) to decompression melting (high Ta/Th; Fig 1b), with a concommittant shift in parental melt Ta/Th from low to high values.

5 Conclusions

We use idealized 1D transport models to provide a strong argument for reassessing the role of open-system interactions between channelized melt and its surrounding wallrock in driving trace element chemical and isotopic equilibration. Within the continental lithospheric mantle (CLM), where melt transport is likely to be channelized, our models constrain the relative importance of mass exchange across channel walls driven by both diffusion and reactive assimilation processes. We show that configurational anisotropy due to the presence of high-diffusivity grain boundaries may enhance the effective diffusivity of the wallrock, however, diffusion alone cannot drive partial equilibration between infiltrating melts and the CLM. Instead, for geologically-reasonable parameters, we show that reactive assimilation is required for partial equilibration between channelized melts and the CLM. The models are used to explore the implications of observed Nd isotopic compositions and Ta/Th ratios in Cenozoic basalts from southwestern North America. Specifically, we show that partial equilibration of Nd isotopes during transport of parental melts through the CLM provides a mechanism to explain the observation of primitive basalts that have simultaneously low Ta/Th and low ε_{Nd}.

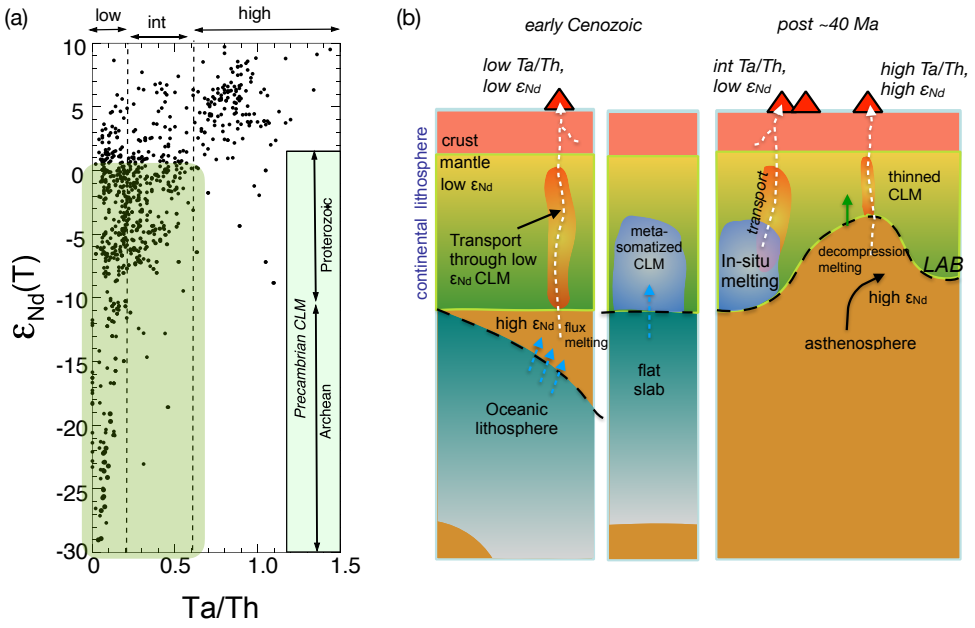

Figure 1. (a). ε_{Nd} vs Ta/Th in Cenozoic basalts with SiO_2<52 wt% within SWNA (small black dots, N=1528, from Farmer et al. (2020)). Green boxes indicate range of ε_{Nd} observed in Cenozoic basalts ascending through older portions of the CLM, with ages as indicated. (b) Cartoon showing possible relationships between Cenozoic basalt Ta/Th and Nd isotopic compositions (ε_{Nd}) and CLM in regions underlain by Precambrian lithosphere in SWNA. *Left:* At end of the Cretaceous Era, thick low ε_{Nd} mantle lithosphere was underlain by the subducted oceanic Farallon plate. Hydrous fluids and volatiles drove flux melting in high ε_{Nd} asthenosphere, producing low Ta/Th in resulting basalts, which bear a low ε_{Nd} signature that may be a result of transport through thick CLM (as investigated here). *Middle:* Fluids from a low-angle subducted plate may have variably metasomatized the overlying CLM. *Right:* After removal of the Farallon slab, eruption of variable ε_{Nd} basalts may be due to *in situ* melting of metasomatized CLM (low ε_{Nd}, intermediate Ta/Th) and by upwelling and decompression melting of asthenosphere beneath thinned CLM (high ε_{Nd} and high Ta/Th). In each case, orange halos indicate zones where parental melts may interact extensively with CLM during ascent, as explored in our modeling.

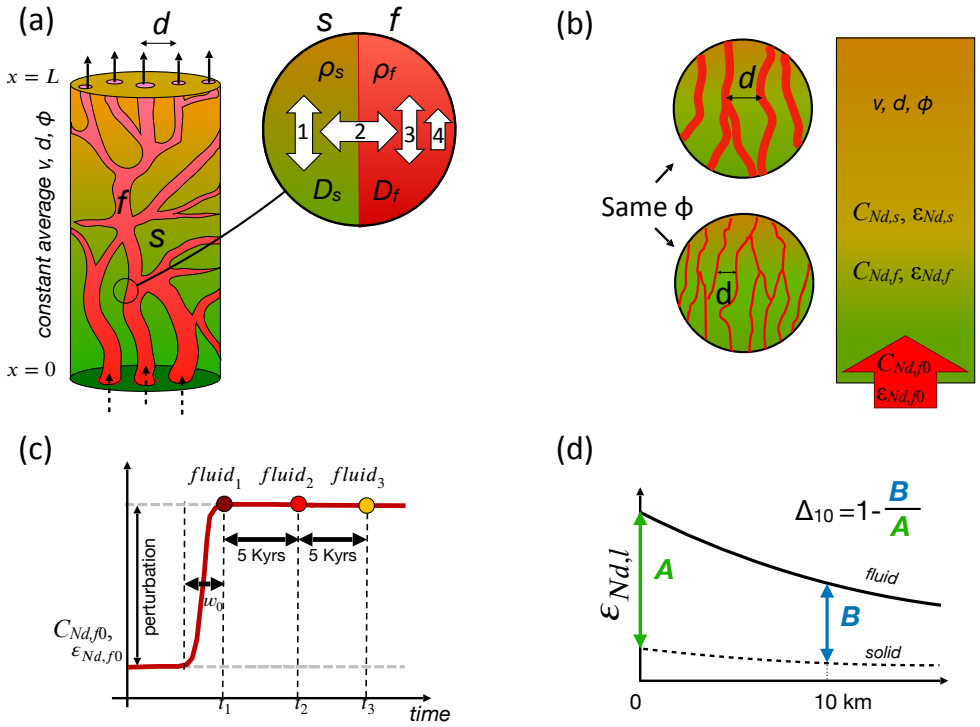

Figure 2. (a) Diagram of melt-rich channels ("fluid"=f, reddish) within a melt-poor region ("solid"=s, greenish). Melt-rich channels are spaced an average distance d apart with volume fraction ϕ; material in the channels has an average velocity v relative to the surrounding rock. The complex melt-transport system is idealized in a 1D model, valid over a length scale where d and ϕ maybe considered nearly constant, and which includes processes: (1) diffusion within the solid, (2) solid-fluid diffusion across the interface, (3) diffusion within the fluid, and (4) fluid advection. (b) Idealized 1D model with channel geometry parameterized by d, ϕ, and channel material velocity, v. As illustrated, changing d with a fixed ϕ is equivalent to changing the interphase contact area per unit volume, following Roy (2022). (c) illustrates a step-like perturbation (with rise-time w_0) in ε_{Nd} and C_f imposed (only) within the incoming channel material at the inlet ($x = 0$). We define t_1 (maroon) as the first time the inlet value reaches the maximum perturbation (e.g., ε_{Nd} reaches +8), and $fluid_1$ as the fluid parcel that enters the domain at t_1. In Fig. 4, we track the evolution of this parcel along with $fluid_2$ and $fluid_3$, entering at $t_2 = t_1 + 5$ Kyrs (red), and $t_3 = t_1 + 10$ Kyrs (yellow). (d) Definition of the degree of equilibration after 10 km of transport, Δ_{10}, illustrated in Fig 4 and 5a, based on the evolution of $fluid_1$ as it enters the domain.

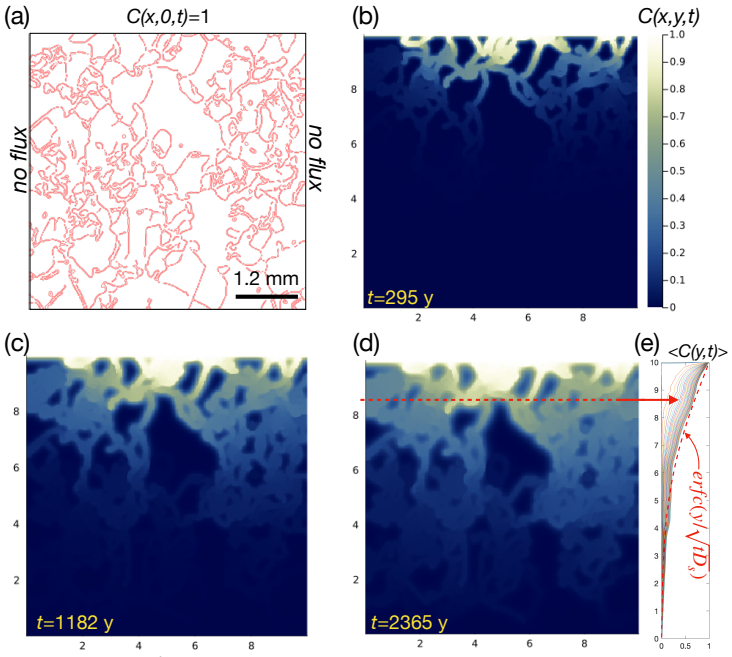

Figure 3. (a) Computational domain spanning ≈7-10 grains (256×256 elements) representing a random grain boundary configuration (red=grain boundaries, white=crystals), where crystals have a lattice diffusivity D_x and grain boundaries have a GB diffusivity D_{GB}=$10^4 D_x$. The configuration of grains is digitized from a peridotite thin-section (from http://microckscopic.ro/). We solve the 2D diffusion equation for (dimensionless) concentration subject to boundary conditions shown on (a) and initial condition $C(x, y, t{=}0){=}0$ everywhere (see Supplementary text S4 for details). (b)-(d): Evolution of $C(x, y, t)$ for times indicated (these times are based on assuming the minimum D_x, 10^{-19} m^2/s), showing anisotropic diffusion into the domain. (e) Row-averaged concentration (direction of averaging indicated on (d)) through time with an effective diffusivity estimated by fitting $erfc(y/\sqrt{tD_s})$ (red dashed line) to the concentration profile at time t.

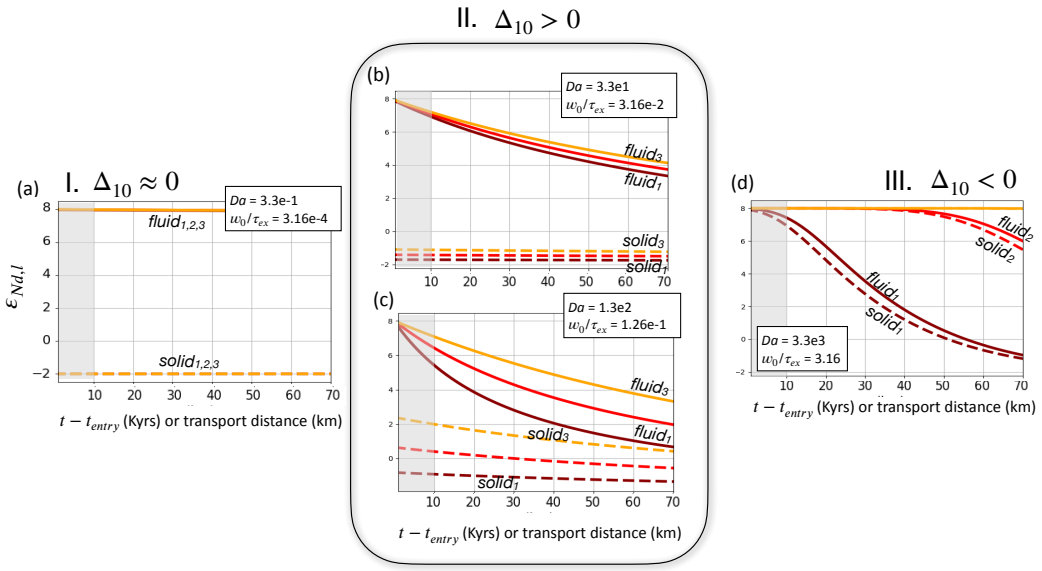

Figure 4. Tracking (Lagrangian) fluid isotopic evolution in response to a smoothed step-perturbation in both $C_{Nd,f}$ and $\varepsilon_{Nd,f}$, within fluid parcels that enter the domain with $\varepsilon_{Nd,l}$ of +8 (indicated as $fluid_1$, $fluid_2$, and $fluid_3$ as in Fig. 2c; corresponding profiles for $C_{Nd,fl}$ and $C_{Nd,sl}$ are provided in Figure S1). Profiles of $\varepsilon_{Nd,l,f}$ (solid lines), as well as the $\varepsilon_{Nd,L,s}$ adjacent to the parcel (dashed) are shown vs time since entry ($t - t_{entry}$). For relative fluid-solid velocity v=1 m/yr, in a Lagrangian reference frame the time since entry in Kyrs is (relative distance traveled in km)/v; therefore, the numbers on the $x-$axis of the plots can also be read as transport distance, in km. Results are shown for varying Da and $\tau' = w_0/\tau_{ex}$, as indicated; other parameters are as in Table 1: $\phi = 0.1$, $D_f = 10^{-11}$ m^2/s, $D_s = 10^{-17}$ m^2/s, $w_0 = 1$ Kyr, $K = 0.0066$. In each case, the degree of equilibration after 10 km of transport (shaded gray region), Δ_{10} is indicated for $fluid_1$ (definition in upper left frame and in text). Three regimes of behavior are evident: (I) $\Delta_{10} \approx 0$ (in (a), no equilibration), (II) $\Delta_{10} > 0$ (in (b) and (c), partial equilibration), (III) $\Delta_{10} < 0$ (in (d), local equilibrium). Corresponding profiles of $\varepsilon_{Nd,f}$ and $\varepsilon_{Nd,s}$ vs position in a domain-fixed reference frame (Eulerian) at different times are shown in Supplementary Fig. S3.

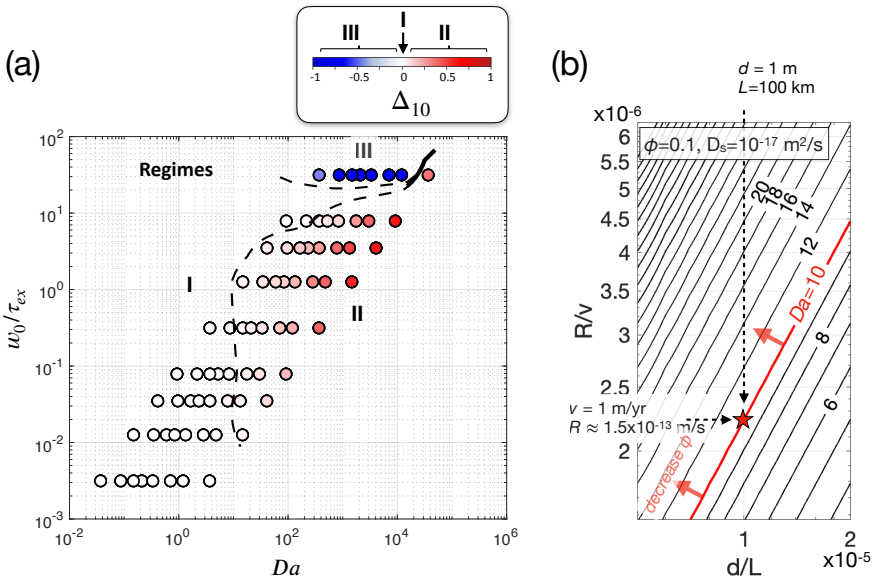

Figure 5. (a) Heat map of the degree of equilibration after 10 km of transport, Δ_{10}, as a function of dimensionless numbers Da and τ', assuming constant: v=1 m/yr, D_f=10^{-11} m^2/s, D_s=10^{-17} m^2/s, w_0=1 Kyr, K=0.0066. Regimes I, II, and III (dashed black lines) are determined as discussed in the text. (b) Contours of Da as a function of dimensionless channel spacing d/L and dimensionless reaction rate R/v. The red star on the Da=10 contour corresponds to $d = 1$ m (for domain length L=100 km), v=1 m/yr and $R = 1.5 \times 10^{-13}$ m/s for a model with $\phi = 0.1$, $D_s = 10^{-17}$ m^2/s, $w_0 = 1$ Kyr, and $K = 0.0066$.

Table 1. Material properties and Nd diffusion constants used in calculations

Name	Symbol	Value or Range	Source/Comments
Nd concentration in solid	C_s	1 ppm	Byerly & Lassiter (2012)
Nd concentration in fluid	C_f	30 ppm	See Suppl S2
ε_{Nd} solid (CLM)	$\varepsilon_{Nd,s}$	-2	(-10) to (-2), D. J. DePaolo & Daley (2000)
ε_{Nd} fluid (Asthenosphere)	$\varepsilon_{Nd,f}$	+8	+7 to +9, D. J. DePaolo & Daley (2000)
Bulk mineral-melt partition coefficient	K_{Nd}	0.0066	Salters & Longhi (1999), composition from Farmer et al. (2020)
In-channel melt velocity	$v_{channel}$	1 m/yr	1 to 10^2 m/yr, Katz et al. (2022)
{fluid, solid} Density	$\{\rho_f, \rho_s\}$	{2800, 3300} kg/m^3	Lesher & Spera (2015)
Channel flow coefficient	α	10	Bodinier et al. (1990); Hauri (1997)
Separation of melt-rich channels	d	1 to 10^2 m	10^{-1} to 10^3 m, LeRoux et al. (2008); Braun & Kelemen (2002)
Volume fraction of melt-rich channels	ϕ	0.05 to 0.2	Liu and Liang (2017)
Nd diffusivity in fluid	D_f	10^{-11} m^2/s	Lesher (1994)
Nd diffusivity in crystals	D_x	10^{-19} to 10^{-17} m^2/s	Tirone et al. (2005); VanOrman et al. (2002); Ganguly et al. (1998)
Solid (grain boundary) diffusivity	D_{GB}	$10^4 D_x$	$D_{GB}/D_x = 10^{3-8}$, Hiraga et al. (2007a,b); Shewmon (1989)
Linear reaction rate	R	10^{-14} to 10^{-13} m/s	required to achieve $Da = [0, 30]$ in Fig 5b
Effective solid diffusivity	D_s	$D_s = 10^{-17}$ m^2/s	following Hiraga et al. (2007b) and Fig 3
Fluid perturbation rise time	w_0	1 kyr	

Citations in Supplementary Information: D. DePaolo & Wasserburg (1976); Walker et al. (2006)

Open Research

Trace element geochemical data used in this study are identical to that in Farmer et al. (2020), with the criterion of wt. % SiO_2 <52. These data are originally available from the NAVDAT/EarthChem database (http://portal.earthchem.org/ using the geographic and temporal criteria for Cenozoic basalts in southwestern North America). The models use Python and Julia; the codes are available at public repository, Roy (2024).

Acknowledgments

We thank thoughtful and detailed comments from two anonymous reviewers. We also thank A. Clark and T. Wickland for discussions and comments in the early stages of this study, and J. van Orman for discussions related to trace element diffusion in ultramafic rocks. This work was supported by NSF via grants EAR-2052909 and EAR-2120812 to MR.

References

Alard, O., Halimulati, A., & Demouchy, S. (2022). Look between the grains. *Nature*

Geoscience, *15*(11), 856–857.

Bodinier, J. L., Vasseur, G., Vernieres, J., Dupuy, C., & Fabries, J. (1990). Mechanisms of mantle metasomatism: Geochemical evidence from the lherz orogenic peridotite. *Journal of Petrology*, *31*, 597-628.

Braun, M., & Kelemen, P. (2002). Dunite distribution in the oman ophiolite: Implications for melt flux through porous dunite conduits. *Geochemistry, Geophysics, Geosystems*, *3*(11).

Byerly, B., & Lassiter, J. (2012). Evidence from mantle xenoliths for lithosphere removal beneath the central rio grande rift. *EPSL*.

Chauvel, C., Lewin, E., Carpentier, M., Arndt, N. T., & Marini, J.-C. (2008). Role of recycled oceanic basalt and sediment in generating the hf–nd mantle array. *Nature geoscience*, *1*(1), 64–67.

Chin, E. J., Lee, C.-T. A., & Barnes, J. D. (2014). Thickening, refertilization, and the deep lithosphere filter in continental arcs: Constraints from major and trace elements and oxygen isotopes. *Earth and Planetary Science Letters*, *397*, 184–200.

Demouchy, S., & Alard, O. (2021). Hydrogen, trace, and ultra-trace element distribution in natural olivines. *Contributions to Mineralogy and Petrology*, *176*(4), 26.

DePaolo, D., & Wasserburg, G. (1976). Nd isotopic variations and petrogenetic models. *GRL*, *3*(5).

DePaolo, D. J., & Daley, E. E. (2000). Neodymium isotopes in basalts of the southwest basin and range and lithospheric thinning during continental extension. *Chemical Geology*, *169*, 157-185.

Dohmen, R., & Milke, R. (2010, 01). Diffusion in Polycrystalline Materials: Grain Boundaries, Mathematical Models, and Experimental Data. *Reviews in Mineralogy and Geochemistry*, *72*(1), 921-970. Retrieved from `https://doi.org/10.2138/rmg.2010.72.21` doi: 10.2138/rmg.2010.72.21

Du, J., A.Haley, B., C.Mix, A., N.Abbott, A., JamesMcManus, & Vance, D. (2022). Reactive-transport modeling of neodymium and its radiogenic isotope in deep-sea sediments: The roles of authigenesis, marine silicate weathering and reverse weathering. *Earth and Planetary Science Letters*, *596*(https://doi.org/10.1016/j.epsl.2022.117792).

Farmer, G. L. (2022). *Reassessing the role of continental lithospheric mantle in*

cenozoic magmatism, southwestern north america. Wiley.

Farmer, G. L., & DePaolo, D. J. (1997). Geochemistry of hydrothermal ore deposits. In (3rd ed., p. 31-62). Barnes.

Farmer, G. L., Fritz, D., & Glazner, A. F. (2020). Identifying metasomatized continental lithospheric mantle involvement in cenozoic magmatism from ta/th values, southwestern north america. *Geochemistry, Geophysics, Geosystems*, *21*, e2019GC008499. https://doi.org/10.1029/2019GC008499.

Fitton, J. G., James, D., Kempton, P., Ormerod, D., & Leeman, W. (1988). The role of lithospheric mantle in the generation of late cenozoic basic magmas in the western united states. *Journal of Petrology*(1), 331–349.

Ganguly, J., Tirone, M., & Hervig, R. L. (1998). Diffusion kinetics of samarium and neodymium in garnet, and a method for determining cooling rates of rocks. *Science*, *281*, 805-807.

Hauri, E. (1997). Melt migration and mantle chromatography, 1: simplified theory and conditions for chemical and isotopic decoupling. *EPSL*, *153*, 1-19.

Hiraga, T., Anderson, I. M., & Kohlstedt, D. L. (2004). Grain boundaries as reservoirs of incompatible elements in the earth's mantle. *Nature*, *427*(6976), 699–703.

Hiraga, T., Hirschmann, M. M., & Kohlstedt, D. L. (2007a). Equilibrium interface segregation in the diopside–forsterite system i: Analytical techniques, thermodynamics, and segregation characteristics. *Geochimica et Cosmochimica Acta*, *71*, 1281-1289.

Hiraga, T., Hirschmann, M. M., & Kohlstedt, D. L. (2007b). Equilibrium interface segregation in the diopside–forsterite system ii: Applications of interface enrichment to mantle geochemistry. *Geochimica et Cosmochimica Acta*, *71*, 1281-1289.

Hirth, G., & Kohlstedt, D. L. (2003, Dec). Rheology of the upper mantle and the mantle wedge: A view from the experimentalists. *Geophysical Monograph Series*, *138*, 83–105.

Iwamori, H. (1993). A model for disequilibrium mantle melting incorporating melt transport by porous and channel flows. *Nature*, *366*(6457), 734–737.

Jaseliūnaitė, J., Povilaitis, M., & Galdikas, A. (2022). Kinetic modeling of grain boundary diffusion: Typical, bi-modal, and semi-lamellar polycrystalline coating morphologies. *Coatings*, *12*(7).

Johnson, T., & DePaolo, D. (1994). Interpretation of isotopic data in groundwater

rock systems: Model development and application to sr isotope data from yucca mountain. *Water Resources Research*, *30*(5), 1571-1587.

Katz, R., Jones, D., Rudge, J., & Keller, T. (2022). Physics of melt extraction from the mantle: Speed and style. *Annual Reviews of Earth and Planetary Sciences*, *50*, 507-540.

Kenyon, P. (1993). Trace elements in migrating high-temperature fluids: Effects of diffusive exchange with the adjoining solid. *JGR*, *98*, 22,007-22,020.

LeRoux, V., Bodinier, J., Tommasi, A., Alard, O., Dautria, J., Vauchez, A., & Riches, A. (2007). The lherz spinel lherzolite: Refertilized rather than pristine mantle. *Earth and Planetary Science Letters*, *259*, 599–612.

LeRoux, V., Bodinier, J.-L., Alard, O., & S.Y. O'Reilly, W. G. (2008). Isotopic decoupling during porous melt flow: A case-study in the lherz peridotite. *Earth and Planetary Science Letters*, *279*, 76-85.

Lesher, C. E. (1994). Kinetics of sr and nd exchange in silicate liquids: Theory, experiments, and applications to uphill diffusion, isotopic equilibration, and irreversible mixing of magmas. *JGR*, *99*(B5), 9585-9604.

Lesher, C. E. (2010). Self-diffusion in silicate melts: Theory, observations and applications to magmatic systems. *Reviews in Mineralogy and Geochemistry*, *72*, 269-309.

Lesher, C. E., & Spera, F. J. (2015). Thermodynamic and transport properties of silicate melts and magma. In (2nd ed., chap. 5). Academic Press.

Liang, Y. (2003). Kinetics of crystal-melt reaction in partially molten silicates: 1. grain scale processes. *Geochemistry, Geophysics, Geosystems*, *4*(5).

Liang, Y., Schiemenz, A., Hesse, M., Parmentier, E. M., & Hesthaven, J. S. (2010). High-porosity channels for melt migration in the mantle: Top is the dunite and bottom is the harzburgite and lherzolite. *GRL*, *37*.

Liu, B., & Liang, Y. (2017). The prevalence of kilometer-scale heterogeneity in the source region of morb upper mantle. *Science*, *3*.

McCulloch, M. T., & Gamble, J. (1991). Geochemical and geodynamical constraints on subduction zone magmatism. *Earth and Planetary Science Letters*, *102*(3-4), 358–374.

Menzies, M. A., Leeman, W. P., & Hawkesworth, C. J. (1983). Isotope geochemistry of cenozoic volcanic rocks reveals mantle heterogeneity below western usa. *Nature*,

303(5914), 205–209.

Navon, O., & Stolper, E. (1987). Geochemical consequences of melt percolation: the upper mantle as a chromatographic column. *Journal of Geology*, *95*(3), 285-307.

Oliveira, B., Afonso, J. C., & Tilhac, R. (2020). A disequilibrium reactive transport model for mantle magmatism. *Journal of Petrology*, *61*(9), egaa067.

Peate, D. W., Pearce, J. A., Hawkesworth, C. J., Colley, H., Edwards, C. M., & Hirose, K. (1997). Geochemical variations in vanuatu arc lavas: the role of subducted material and a variable mantle wedge composition. *Journal of Petrology*, *38*(10), 1331–1358.

Reddy, S. M., Saxey, D. W., Rickard, W. D., Fougerouse, D., Montalvo, S. D., Verberne, R., & Van Riessen, A. (2020). Atom probe tomography: Development and application to the geosciences. *Geostandards and Geoanalytical Research*, *44*(1), 5–50.

Roy, M. (2022). Assessing the role of thermal disequilibrium in the evolution of the lithosphere-asthenosphere boundary: An idealized model of heat exchange during melt-transport. *JGR Solid Earth*.

Roy, M. (2024). mousumiroy-unm/endmelttransport: v1.0.1 (v1.0.1). *Zenodo*(https://doi.org/10.5281/zenodo.13732506).

Salters, V. J., & Longhi, J. (1999). Trace element partitioning during the initial stages of melting beneath mid-ocean ridges. *Earth and Planetary Science Letters*, *166*(1-2), 15-30.

Shewmon, P. (1989). Diffusion in solids. The Minerals, Metals, and Materials Society.

Soustelle, V., A.Tommasi, Bodinier, J. L., Garrido, C. J., & A.Vauchez. (2009). Deformation and reactive melttransport in the mantle lithosphere above a large-scale partial melting domain: the ronda peridotite massif, southern spain. *Journal of Petrology*, *50*(7), 1235-1266.

Stracke, A. (2021). A process-oriented approach to mantle geochemistry. *Chemical Geology*, *579*, 120350.

Stracke, A., & Bourdon, B. (2009). The importance of melt extraction for tracing mantle heterogeneity. *Geochimica et Cosmochimica Acta*, *73*(1), 218-238.

Tirone, M., Ganguly, J., Dohmen, R., Langenhorst, F., Hervig, R., & Becker, H.-W. (2005). Rare earth diffusion kinetics in garnet: experimental studies and

applications. *Geochimica et Cosmochimica Acta*, *69*(9), 2385–2398.

Van Orman, J. A., Grove, T. L., & Shimizu, N. (1998). Uranium and thorium diffusion in diopside. *Earth and Planetary Science Letters*, *160*(3-4), 505–519.

VanOrman, J. A., Grove, T. L., Shimizu, N., & Layne, G. D. (2002). Rare earth element diffusion in a natural pyrope crystal at 2.8 gpa. *Contrib Mineral Petrol*, *142*, 416-424.

Walker, J., Bowers, T., Black, R., Glazner, A., Farmer, G., & Carlson, R. (2006). A geochemical database for western north american volcanic and intrusive rocks (navdat). *Special Paper - Geological Society of America*, *397*, 61-71.

Watkins, J. M., DePaolo, D. J., Ryerson, F. J., & Peterson, B. T. (2011). Influence of liquid structure on diffusive isotope separation in molten silicates and aqueous solutions. *Geochimica et Cosmochimica Acta*, *75*, 3103-3118.

Watkins, J. M., DePaolo, D. J., & Watson, E. B. (2017). Kinetic fractionation of non-traditional stable isotopes by diffusion and crystal growth reactions. *Reviews in Mineralogy and Geochemistry*, *82*, 85-125.

Watkins, J. M., Liang, Y., Richter, F., Ryerson, F. J., & DePaolo, D. J. (2014). Diffusion of multi-isotopic chemical species in molten silicates. *Geochimica et Cosmochimica Acta*, *139*, 313–326.

Zhang, Y. (2010). Diffusion in minerals and melts: Theoretical background. *Reviews in Mineralogy and Geochemistry*, *72*, 5-59.

Supporting Information for "Nd isotopic equilibration during channelized melt transport through the lithosphere: a feasibility study using idealized numerical models"

Mousumi Roy[1], G. Lang Farmer[2], and Kellen Malone[1]

[1]Department of Physics and Astronomy, University of New Mexico, Albuquerque, NM 87109, USA

[2]Department of Geological Sciences and CIRES, University of Colorado Boulder, Boulder, CO, USA

Contents of this file

S1. Mole fraction evolution equations

To derive equations for the mole fraction f in the fluid and solid, we start with the pair of modified advection-diffusion equations for the concentration of total Nd in the fluid and solid and define the LHS sides to equal to some gradients in flux $-\partial J/\partial x$:

$$\frac{\partial C_f(x,t)}{\partial t} + v\frac{\partial C_f(x,t)}{\partial x} = -\frac{(1-\phi)\rho_s}{\phi\rho_f}\frac{1}{\tau_{ex}}(KC_f(x,t) - C_s(x,t)) + D_f\frac{\partial^2 C_f(x,t)}{\partial x^2} \equiv -\frac{\partial J_f}{\partial x} \tag{1}$$

$$\frac{\partial C_s(x,t)}{\partial t} = \frac{1}{\tau_{ex}}(KC_f(x,t) - C_s(x,t)) + D_s\frac{\partial^2 C_s(x,t)}{\partial x^2} \equiv -\frac{\partial J_s}{\partial x} \tag{2}$$

We are only considering 2 Nd isotopes in the fluid and solid:

$$C = C^{143} + C^{144} \tag{3}$$

The LHS of Eqns (1) and (2) after expanding by isotope are:

$$\frac{\partial C_f(x,t)}{\partial t} + v\frac{\partial C_f(x,t)}{\partial x} = \frac{\partial C_f^{143}(x,t)}{\partial t} + v\frac{\partial C_f^{143}(x,t)}{\partial x} + \frac{\partial C_f^{144}(x,t)}{\partial t} + v\frac{\partial C_f^{144}(x,t)}{\partial x} \tag{4}$$

$$\frac{\partial C_s(x,t)}{\partial t} = \frac{\partial C_s^{143}(x,t)}{\partial t} + \frac{\partial C_s^{144}(x,t)}{\partial t} \tag{5}$$

We then expand the RHS of (1) and (2) and separate out the flux into isotopic components

$$-\frac{\partial J_f}{\partial x} = -\frac{\partial J_f^{143}}{\partial x} - \frac{\partial J_f^{144}}{\partial x} \tag{6}$$

$$-\frac{\partial J_s}{\partial x} = -\frac{\partial J_s^{143}}{\partial x} - \frac{\partial J_s^{144}}{\partial x} \tag{7}$$

20 Then equating same isotopes

$$\frac{\partial C_f^{144}}{\partial t} + v\frac{\partial C_f^{144}}{\partial x} = -\frac{(1-\phi)\rho_s}{\phi\rho_f}\frac{1}{\tau_{ex}}(KC_f^{144}(x,t) - C_s^{144}(x,t)) + D_f\frac{\partial^2 C_f^{144}(x,t)}{\partial x^2} = -\frac{\partial J_f^{144}}{\partial x} \tag{8}$$

$$\frac{\partial C_f^{143}}{\partial t} + v\frac{\partial C_f^{143}}{\partial x} = -\frac{(1-\phi)\rho_s}{\phi\rho_f}\frac{1}{\tau_{ex}}(KC_f^{143}(x,t) - C_s^{143}(x,t)) + D_f\frac{\partial^2 C_f^{143}(x,t)}{\partial x^2} = -\frac{\partial J_f^{143}}{\partial x} \tag{9}$$

$$\frac{\partial C_s^{144}}{\partial t} = \frac{1}{\tau_{ex}}(KC_f^{144}(x,t) - C_s^{144}(x,t)) + D_s\frac{\partial^2 C_s^{144}(x,t)}{\partial x^2} = -\frac{\partial J_s^{144}}{\partial x} \tag{10}$$

$$\frac{\partial C_s^{143}}{\partial t} = \frac{1}{\tau_{ex}}(KC_f^{143}(x,t) - C_s^{143}(x,t)) + D_s\frac{\partial^2 C_s^{143}(x,t)}{\partial x^2} = -\frac{\partial J_s^{143}}{\partial x} \tag{11}$$

21 Next we substitute the isotopic concentrations with

$$C^{143}(x,t) = (1 - f(x,t))C(x,t) \tag{12}$$

$$C^{144}(x,t) = f(x,t)C(x,t) \tag{13}$$

22 and using the product rule we get

$$\frac{\partial C_f^{144}(x,t)}{\partial t} + v\frac{\partial C_f^{144}(x,t)}{\partial x} = f_f\left(\frac{\partial C_f}{\partial t} + v\frac{\partial C_f}{\partial x}\right) + C_f\left(\frac{\partial f_f}{\partial t} + v\frac{\partial f_f}{\partial x}\right) = -\frac{\partial J_f^{144}}{\partial x} \tag{14}$$

$$\frac{\partial C_s^{144}(x,t)}{\partial t} = f_s\left(\frac{\partial C_s}{\partial t}\right) + C_s\left(\frac{\partial f_s}{\partial t}\right) = -\frac{\partial J_s^{144}}{\partial x} \tag{15}$$

and equivalently for the other isotope. The LHS of (14) and (15) are replaced with the gradient in flux and rearranged.

$$\frac{\partial f_f}{\partial t} + v\frac{\partial f_f}{\partial x} = \frac{1}{C_f}\left(-\frac{\partial J_f^{144}}{\partial x} + f_f\frac{\partial J_f}{\partial x}\right) \tag{16}$$

$$\frac{\partial f_s}{\partial t} = \frac{1}{C_s}\left(-\frac{\partial J_f^{144}}{\partial x} + f_s\frac{\partial J_s}{\partial x}\right) \tag{17}$$

The isotopic fluxes are replaced with their equivalent exchange and diffusion terms.

$$\frac{\partial f_f}{\partial t} + v\frac{\partial f_f}{\partial x} = \frac{1}{C_f}\left(-\frac{(1-\phi)\rho_s}{\phi\rho_f}\frac{1}{\tau_{ex}}(KC_f^{144}(x,t) - C_s^{144}(x,t)) + D_f\frac{\partial^2 C_f^{144}(x,t)}{\partial x^2} + f_f\frac{\partial J_f}{\partial x}\right) \tag{18}$$

$$\frac{\partial f_s}{\partial t} = \frac{1}{C_s}\left(\frac{1}{\tau_{ex}}(KC_f^{144}(x,t) - C_s^{144}(x,t)) + D_s\frac{\partial^2 C_s^{144}(x,t)}{\partial x^2} + f_s\frac{\partial J_s}{\partial x}\right) \tag{19}$$

Substituting the isotopic concentrations with the product of f and C and expanding with the product rule yields the final equations for f.

$$\frac{\partial f_f}{\partial t} + v\frac{\partial f_f}{\partial x} = \frac{1}{C_f}\left(-\frac{(1-\phi)\rho_s}{\phi\rho_f}\frac{1}{\tau_{ex}}C_s(f_f - f_s) + 2D_f\frac{\partial f_f}{\partial x}\frac{\partial C_f}{\partial x} + D_f\frac{\partial^2 f_f}{\partial x^2}C_f\right) \tag{20}$$

$$\frac{\partial f_s}{\partial t} = \frac{1}{C_s}\left(\frac{1}{\tau_{ex}}KC_f(f_f - f_s) + 2D_s\frac{\partial f_s}{\partial x}\frac{\partial C_s}{\partial x} + D_s\frac{\partial^2 f_s}{\partial x^2}C_s\right) \tag{21}$$

$(1-f)/f$ then gives the concentration of $^{143}\mathrm{Nd}/^{144}\mathrm{Nd}$ in the fluid or solid.

$$\frac{1-f}{f} = \frac{^{143}\mathrm{Nd}}{^{144}\mathrm{Nd}} \tag{22}$$

S2. Chemical and isotopic perturbations

We choose the modal concentration from Cenozoic basalts in SWNA (30 ppm; Fig S3), as the perturbation imposed on fluid entering at $t > 0$, after an initial steady state. Nd concentration in the solid is based on mantle xenoliths of (Byerly & Lassiter, 2012) and for this work is taken to be 1 ppm. The conversion from ppm Nd to mol fraction is as follows:

$$\frac{30 * 10^{-6} \text{ g Nd}}{1 \text{ g rock}} * \frac{1 \text{ mol Nd}}{144 \text{ g Nd}} * \frac{1000 \text{ g}}{1 \text{ kg}} * \frac{2800 \text{ kg}}{\text{m}^3} * \frac{23.8 \ ^{144}\text{Nd}}{100 \text{ Nd}} = 0.1388 \frac{\text{mol } ^{144}\text{Nd}}{\text{m}^3} \quad (1)$$

$$\left(\frac{\varepsilon_{Nd,f1}}{10,000} + 1 \right) * I_{CHUR} * 0.1386 \frac{\text{mol } ^{144}\text{Nd}}{\text{m}^3} = 0.07099 \frac{\text{mol } ^{143}\text{Nd}}{\text{m}^3} \quad (2)$$

$$C_{f1} = 0.07099 \frac{\text{mol}^{143}\text{Nd}}{\text{m}^3} + 0.1386 \frac{\text{mol}^{144}\text{Nd}}{\text{m}^3} = 0.2096 \frac{\text{mol Nd}}{\text{m}^3} \quad (3)$$

Where $I_{CHUR} = (^{143}\text{Nd}/^{144}\text{Nd})_{CHUR} = 0.511836$ (DePaolo & Wasserburg, 1976). Similarly, we calculate C_{s0} with an additional step of using an equilibrium condition at the fluid-solid interface to calculate the equilibrium fluid concentration C_{f0}.

$$\frac{1 * 10^{-6} \text{ g Nd}}{1 \text{ g rock}} * \frac{1 \text{ mol Nd}}{144 \text{ g Nd}} * \frac{1000 \text{ g}}{1 \text{ kg}} * \frac{3300 \text{ kg}}{\text{m}^3} * \frac{23.8 \ ^{144}\text{Nd}}{100 \text{ Nd}} = 0.005454 \frac{\text{mol } ^{144}\text{Nd}}{\text{m}^3} \quad (4)$$

$$\left(\frac{\varepsilon_{Nd,f0}}{10,000} + 1 \right) * I_{CHUR} * 0.005454 \frac{\text{mol } ^{144}\text{Nd}}{\text{m}^3} = 0.002791 \frac{\text{mol } ^{143}\text{Nd}}{\text{m}^3} \quad (5)$$

$$C_{s0} = 0.005454 \frac{\text{mol}^{143}\text{Nd}}{\text{m}^3} + 0.002791 \frac{\text{mol}^{144}\text{Nd}}{\text{m}^3} = 0.008245 \frac{\text{mol Nd}}{\text{m}^3} \quad (6)$$

$$C_{f0} = C_{s0}/K = 0.008245 \frac{\text{mol Nd}}{\text{m}^3} / 0.025 = 0.3298 \frac{\text{mol Nd}}{\text{m}^3} \tag{7}$$

S3. Nondimensionalization and numerical methods

To nondimensionalize the Equations (**??**) to (**??**) in the paper, we define a length scale L, the domain length, and time scale $T = d^2/D_s$ and define nondimensional quantities $x' = x/L$ and $t' = t/T$. We define the dimensionless Dahmkohler number Da in Eqn (5) as a weighted ratio of the advective and exchange timescales, τ_{ad} and τ_{ex}. The exchange timescale is a function of both diffusion and reaction parameters (D_s, R) and channel geometry parameters (d and ϕ). This leads to Da varies as illustrated in Fig S1. Substituting $x = x'L$ and $t = t'T$, Eqns (1), (2), (20), and (21) in 1 become:

$$\frac{\partial C_f}{\partial t'} + \frac{\partial C_f}{\partial x'} = -Da(KC_f - C_s) + \frac{D_f}{Lv}\frac{\partial^2 C_f}{\partial x'^2} \tag{1}$$

$$\frac{\partial C_s}{\partial t'} = Da\frac{\phi\rho_f}{(1-\phi)\rho_s}(KC_f - C_s) + \frac{D_s}{Lv}\frac{\partial^2 C_s}{\partial x'^2} \tag{2}$$

$$\frac{\partial f_f}{\partial t'} + \frac{\partial f_f}{\partial x'} = \frac{1}{C_f}\left(-DaC_s(f_f - f_s) + 2\frac{D_f}{Lv}\frac{\partial f_f}{\partial x'}\frac{\partial C_f}{\partial x'} + \frac{D_f C_f}{Lv}\frac{\partial^2 f_f}{\partial x'^2}\right) \tag{3}$$

$$\frac{\partial f_s}{\partial t'} = \frac{1}{C_s}\left(Da\frac{\phi\rho_f}{(1-\phi)\rho_s}KC_f(f_f - f_s) + 2\frac{D_s}{Lv}\frac{\partial f_s}{\partial x'}\frac{\partial C_s}{\partial x'} + \frac{D_s C_s}{Lv}\frac{\partial^2 f_s}{\partial x'^2}\right) \tag{4}$$

The domain length $L = 10^5$ m is discretized into N points with $dx = L/N$, and the total simulation time $t_{max} = 10^5$ yrs is discretized into $N_t = t_{max}/dt$ time steps. The numerical scheme implemented is a finite difference explicit time leapfrog, center space on the dimensional and nondimensional set of equations described above. Values $dx = 0.05$ km and $dt = 0.05$ years ($N = N_t = 2000$) are chosen to eliminate numerical instabilities.

A smoothed step-change $\Delta\varepsilon_{Nd,f}$ in the isotopic composition of the incoming fluid is represented by

$$\varepsilon_{Nd,f}(0,t) = \varepsilon_{Nd,f0} + \frac{\Delta\varepsilon_{Nd,f}}{2}\left(1 + \tanh\left(\frac{t-\sigma}{w_0}\right)\right) \tag{5}$$

where $\varepsilon_{Nd,f0}$ is the initial value and w_0 a characteristic rise time (=1 Kyrs; Table **??**) and delay σ (= $5w_0$; Fig. **??**c). For a given perturbation in $\varepsilon_{Nd,f}(0,t)$, the required perturbation in $f_f(0,t)$ is

$$f_f(0,t) = \left[\left(\frac{\varepsilon_{Nd,f}(0,t)}{10,000} + 1\right) * I_{CHUR} + 1\right]^{-1} \tag{6}$$

where $I_{CHUR} = (^{143}\mathrm{Nd}/^{144}\mathrm{Nd})_{CHUR}$. A change in the chemical composition of the incoming fluid may be represented by a similar smoothed step function:

$$C_f(0,t) = C_{f0} + \frac{\Delta C_f}{2}\left(1 + \tanh\left(\frac{t-\sigma}{w_0}\right)\right) \tag{7}$$

where C_{f0} is the starting value calculated from applying the equilibrium condition between the fluid and the solid concentrations, $KC_{f0} = C_{s0}$, where C_{s0} is taken from mantle xenolith Nd concentrations in (Byerly & Lassiter, 2012). ΔC_f is taken from the mode of NAVDAT basalt Nd abundances (S2). Solutions for the evolution of $\varepsilon_{Nd,f}$ and $\varepsilon_{Nd,s}$ after the imposed perturbations are illustrated as a function of time and position within the domain in Fig S2.

S4. 2D Grain-Scale Model for Effective Diffusivity

To estimate the role of enhanced diffusivity and segregation of trace elements associated with grain boundaries, we set up a simple 2D diffusion calculation within a square domain with dimensionless width and height $L = 10$, discretized into N cells ($N = n_x * n_y$, where $n_x = n_y$ =256, 512, etc.). The model solves the diffusion equation for the evolution of a hypothetical tracer concentration $C(x, y, t)$:

$$\frac{\partial^2 C(x,y,t)}{\partial t^2} = \vec{\nabla} \cdot (D(x,y)\vec{\nabla} C(x,y,t)) \tag{1}$$

using the finite-difference method. The space derivatives utilize the ParallelStencil package (`https://github.com/omlins/ParallelStencil.jl`) in a Julia code. The concentration $C(x, y, t)$ function is obtained subject to an initial condition of $C(x, y, 0 = 0$ everywhere and a boundary condition of $C(x, L, t) = 1$ at the top edge. The diffusivity array $D(x, y)$ is based on the configuration of grains in a thin section of a peridotite (from http://microckscopic.ro/). For each node in the model, we classify it as either within a grain boundary region or within a crystal. We assume that diffusivity in grain boundaries is enhanced by a factor $E = D_{GB}/D_x$ over the lattice value. We also allow for an (optional) segregation factor at grain boundaries. Time evolution utilizes a leapfrog method (see also Roy (2022)), with the time step dt chosen to stabilize the solution. Results in Fig 3 are shown for $n_x = n_y = 256$. We confirm that this resolution is sufficient and the results are independent of discretization (Fig. S4).

References

Byerly, B., & Lassiter, J. (2012). Evidence from mantle xenoliths for lithosphere removal beneath the central rio grande rift. *EPSL*.

DePaolo, D., & Wasserburg, G. (1976). Nd isotopic variations and petrogenetic models. *GRL*, *3*(5).

Farmer, G. L., Fritz, D., & Glazner, A. F. (2020). Identifying metasomatized continental lithospheric mantle involvement in cenozoic magmatism from ta/th values, southwestern north america. *Geochemistry, Geophysics, Geosystems*, *21*, e2019GC008499. https://doi.org/10.1029/2019GC008499.

Roy, M. (2022). Assessing the role of thermal disequilibrium in the evolution of the lithosphere-asthenosphere boundary: An idealized model of heat exchange during melt-transport. *JGR Solid Earth*.

Walker, J., Bowers, T., Black, R., Glazner, A., Farmer, G., & Carlson, R. (2006). A geochemical database for western north american volcanic and intrusive rocks (navdat). *Special Paper - Geological Society of America*, *397*, 61-71.

5. Supplementary Figures

Supplementary Figures S1 to S4.

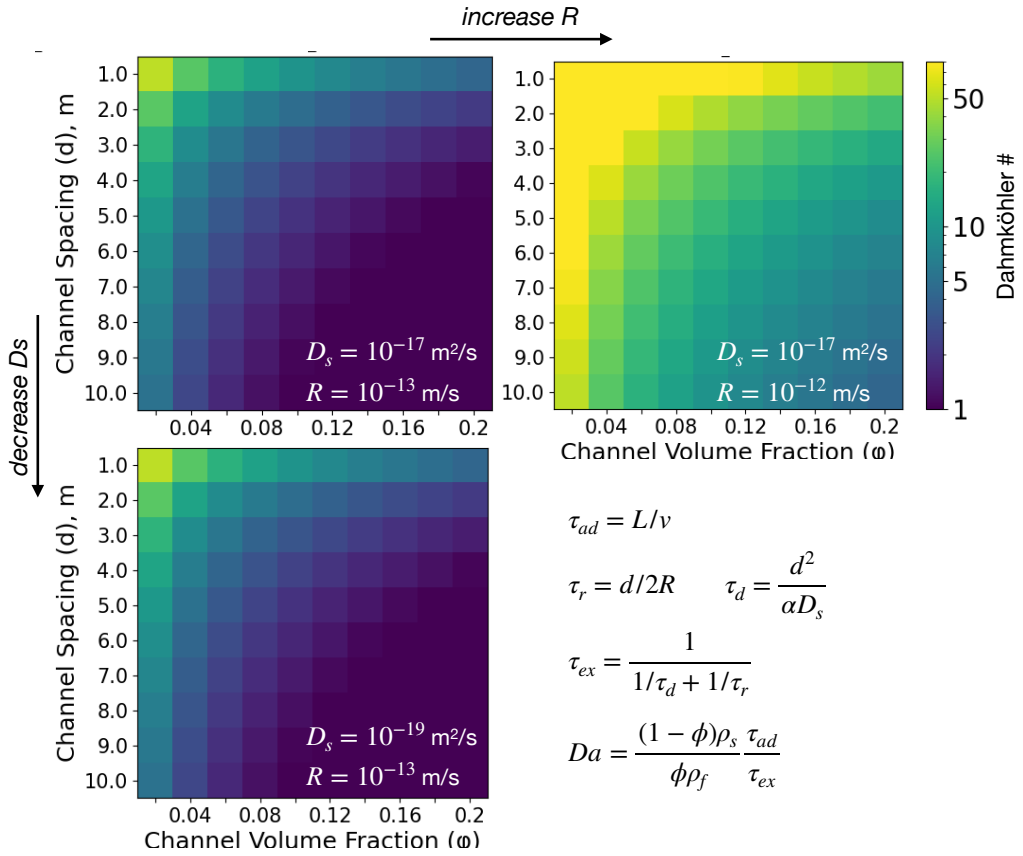

Figure S1. For a domain length L=100 km and relative fluid-solid velocity of v=1 m/yr, the Dahmköhler number is shown for various model parameters as indicated. Overall, it is a stronger function of the linear reaction rate R than the wallrock diffusivity D_s (compare top left panel to bottom and right).

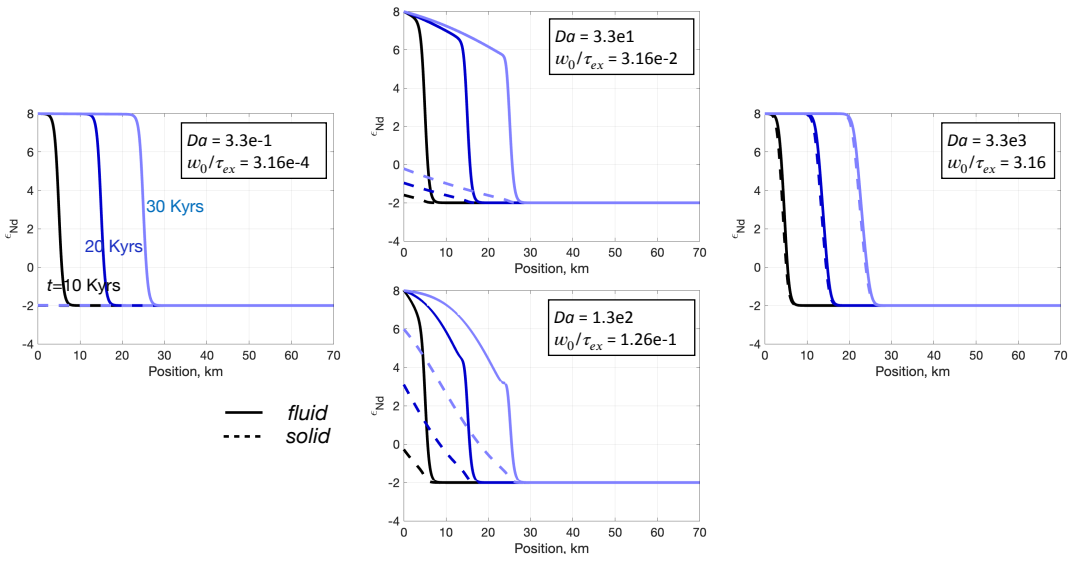

Figure S2. Profiles of $\varepsilon_{Nd,f}$ (solid lines) and $\varepsilon_{Nd,s}$ (dashed lines) as a function of position within the model domain in a fixed (Eulerian) reference frame, plotted at three times as indicated. These profiles, with the Dahmköhler numbers as indicated, correspond to those in Fig. **??** in the text.

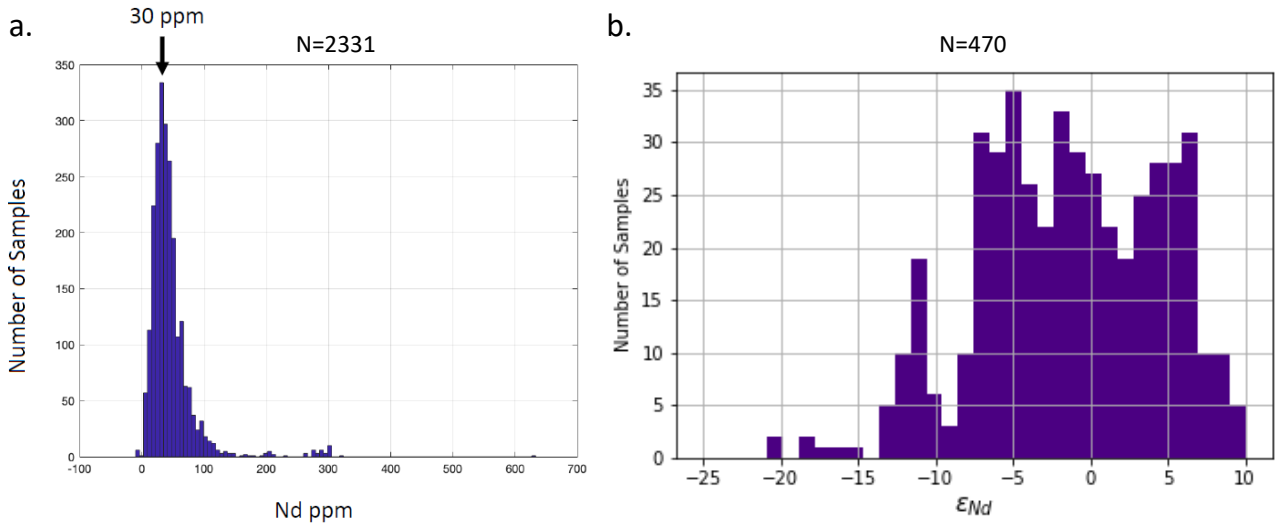

Figure S3. (a) Histogram of the number of basalt samples with a given Nd concentration in ppm from a subset of samples from the NAVDAT database Walker et al. (2006). (b) Histogram of Nd-isotopic composition of low silica basalts in (a) (wt % $SiO_2 \leq 52$ from Farmer et al. (2020)

.

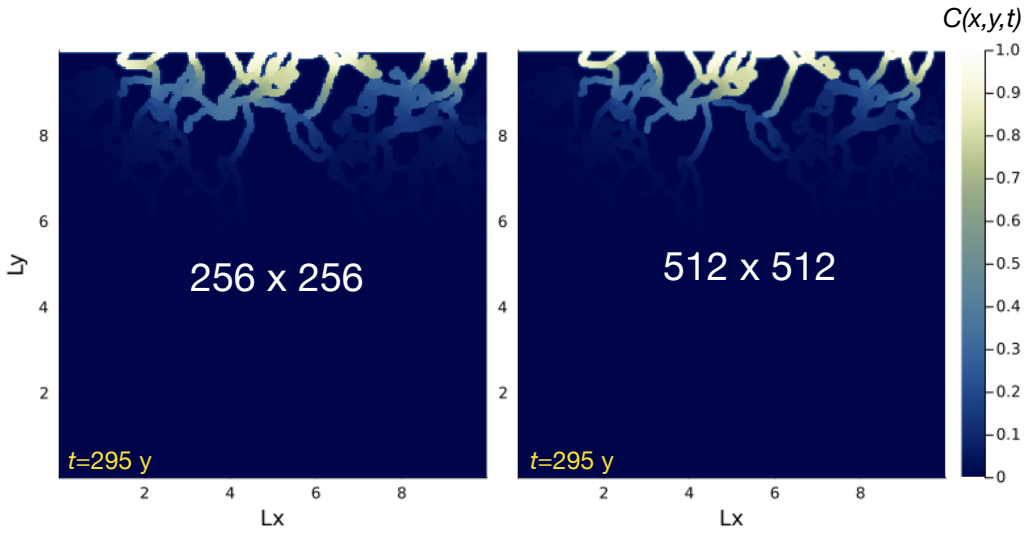

Figure S4. Resolution test comparing model results at equivalent times, but with different resolutions, $n_x = n_y = 256$ (left) vs. $n_x = n_y = 512$.